Microkinetic Modeling for Water-Promoted CO Oxidation, Water–Gas Shift, and Preferential Oxidation of CO on Pt

**A. B. Mhadeshwar and D. G. Vlachos***

Department of Chemical Engineering and Center for Catalytic Science and Technology, University of Delaware, Newark, Delaware 19716-3110

Received: March 23, 2004; In Final Form: July 12, 2004

A comprehensive surface reaction mechanism on Pt is presented that is capable of describing CO oxidation, H_2 oxidation, water–gas shift (WGS), preferential oxidation (PROX) of CO, and the promoting role of H_2O on CO oxidation reasonably well. This mechanism consists of a literature CO oxidation model, a surface reaction mechanism for H_2 oxidation on Pt developed here, and coupling reactions between the CO and H_2 chemistries included for the first time. Thermodynamic consistency, which is shown to be essential for WGS, is ensured in all steps of the entire mechanism. The CO–H_2 coupling via the CO + OH reaction, which may involve direct CO_2 formation, $CO^* + OH^* \leftrightarrow CO_2^* + H^*$, as well as an indirect pathway via the carboxyl intermediate, is explored. It is shown that this coupling plays a significant role in capturing the promoting effect of H_2O on the CO oxidation-temperature-programmed reaction experiments at low temperatures as well as the overall speed of the WGS and PROX reactions. With the parameters used here, the direct path dominates in the water-promoted low-temperature CO oxidation, whereas the indirect path is more or equally important in the WGS and PROX reactions, depending on the operating conditions. Finally, it is found that the facilitation of the disproportionation of H_2O^*, $H_2O^* + O^* \rightarrow 2OH^*$, via hydrogen bonding, is a possible mechanism for low-temperature CO oxidation via the direct path.

Introduction

Hydrogen-based proton-exchange membrane (PEM) fuel cells show good potential for the production of electricity. However, widespread commercialization of PEM fuel cells will depend on cheap and environmentally benign production of H_2. Currently, H_2 is mainly produced from syngas via the water–gas shift (WGS) reaction

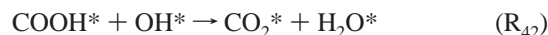$$CO + H_2O \leftrightarrow CO_2 + H_2 \qquad (1)$$
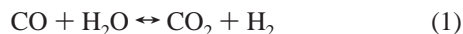
followed by the preferential oxidation (PROX) of CO. While syngas is currently produced by steam reforming of natural gas, the short-contact-time partial oxidation (POX) of syngas over transition metals is a potential alternative.[1,2] Steam reforming of the products of POX and of leftover methane, via the H_2O byproduct downstream of the POX reaction zone, has been speculated to be important in the POX process. These processes share reactants and products and the same underlying H_2 and CO oxidation chemistry on transition metals.

Extensive work has been devoted to the catalytic oxidation of H_2 and CO on transition metals, and a number of microkinetic models, consisting of elementary-like reaction steps, have been proposed, especially on Pt.[3–10] Yet, as we will show, microkinetic models that could be used for the simultaneous modeling of WGS, PROX, and POX reactors are still lacking. Generic shortcomings of microkinetic models are outlined in refs 10–11. In particular, one important aspect entails the thermodynamic inconsistency of kinetic parameters that is common in POX models of syngas and its subsets (i.e., H_2 and CO oxidation) of
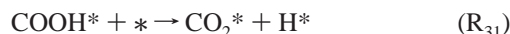
relevance to WGS and PROX processes. A second crucial aspect is the coupling that arises from the use of mixtures of CO and H_2 or CO, O, and H_2O that cannot currently be captured with the available microkinetic models. Recently, a DFT-based microkinetic model for PROX has been proposed (see ref 12), but it does not include any coupling steps. An example of such coupling is the production of oxygenates, such as carboxyl (COOH*), via a recombination reaction

$$CO^* + OH^* \rightarrow COOH^* + * \qquad (R_{30})$$

and its subsequent decomposition

$$COOH^* + OH^* \rightarrow CO_2^* + H_2O^* \qquad (R_{42})$$

or

$$COOH^* + * \rightarrow CO_2^* + H^* \qquad (R_{31})$$

The reaction numbering here corresponds to Table 1, and the asterisk (*) denotes an empty site or an adsorbed species. Formate (HCOO**) also undergoes similar reactions. The presence of such oxygenates in CO–H_2 mixtures has previously been proposed and observed experimentally.[13–16] Recent temperature-programmed reaction (TPR) results[17] provided evidence that even small fractions of H_2O^* have an enhancing effect on CO oxidation at low temperatures. In an attempt to explain the enhancing effect of H_2O, density functional theory (DFT) calculations were performed by Gong and Hu.[18] Their calculations showed that the CO oxidation barrier is reduced in the presence of H_2O. In addition, it was proposed that CO_2

* Corresponding author. Phone: (302)-831-2830. Fax: (302)-831-1048. E-mail: vlachos@che.udel.edu.

Microkinetic Modeling for CO Oxidation

J. Phys. Chem. B, Vol. 108, No. 39, 2004 **15247**

TABLE 1: Surface Reaction Mechanism for H₂ and CO Oxidation and the CO−H₂ Coupling on Pt[a]

no.	reaction	sticking coefficient (unitless) or pre-exponential (s^{-1})	temperature exponent β	activation energy at 300 K (kcal/mol)
		Hydrogen Oxidation on Pt		
R_1	$H_2 + 2* \rightarrow 2H*$	1.29×10^{-1}	0.858	0.0
R_2	$2H* \rightarrow H_2 + 2*$	7.95×10^{12}	−0.001	$19.8 - 6\theta_H + f(T)$
R_3	$O_2 + 2* \rightarrow 2O*$	5.42×10^{-2}	0.766	0.0
R_4	$2O* \rightarrow O_2 + 2*$	8.41×10^{12}	−0.796	$50.9 - 32\theta_O + f(T)$
R_5	$OH* + * \rightarrow H* + O*$	1.95×10^{12}	1.872	$27.1 + f(\theta_O,\theta_H,\theta_{H_2O},T)$
R_6	$H* + O* \rightarrow OH* + *$	6.33×10^{12}	0.624	$8.8 + f(\theta_O,\theta_H,\theta_{H_2O},T)$
R_7	$H_2O* + * \rightarrow H* + OH*$	9.36×10^{12}	−0.118	$17.8 + f(\theta_O,\theta_H,\theta_{OH},\theta_{H_2O},T)$
R_8	$H* + OH* \rightarrow H_2O* + *$	9.99×10^{12}	−1.049	$13.5 + f(\theta_O,\theta_H,\theta_{OH},\theta_{H_2O},T)$
R_9	$H_2O* + O* \rightarrow 2OH*$	4.32×10^9 *4.32×10^{10}*	0.082	$8.8 + f(\theta_O,\theta_{OH},\theta_{H_2O},T)$
R_{10}	$2OH* \rightarrow H_2O* + O*$	1.70×10^9 *1.70×10^{10}*	0.325	$22.7 + f(\theta_O,\theta_{OH},\theta_{H_2O},T)$
R_{11}	$OH + * \rightarrow OH*$	9.99×10^{-1}	2.000	0.0
R_{12}	$OH* \rightarrow OH + *$	1.44×10^{14}	2.000	$63.0 - 33\theta_O + 25\theta_{H_2O} + f(T)$
R_{13}	$H_2O + * \rightarrow H_2O*$	1.08×10^{-1}	1.162	0.0
R_{14}	$H_2O* \rightarrow H_2O + *$	2.03×10^{12}	1.372	$10.0 - 2.5\theta_{H_2O} + 25\theta_{OH} + f(T)$
R_{15}	$H + * \rightarrow H*$	3.84×10^{-1}	1.832	0.0
R_{16}	$H* \rightarrow H + *$	4.37×10^{13}	1.890	$62.0 - 3\theta_H + f(T)$
R_{17}	$O + * \rightarrow O*$	4.91×10^{-2}	0.250	0.0
R_{18}	$O* \rightarrow O + *$	1.44×10^{13}	−0.250	$85.0 - 16\theta_O + f(T)$
		CO Oxidation on Pt		
R_{19}	$CO + * \rightarrow CO*$	1.00×10^0	0.000	0.0
R_{20}	$CO* \rightarrow CO + *$	5.66×10^{15}	−0.500	$40 - 15\theta_{CO} + f(T)$
R_{21}	$CO_2 + * \rightarrow CO_2*$	1.95×10^{-1}	0.250	0.0
R_{22}	$CO_2* \rightarrow CO_2 + *$	3.63×10^{12}	−0.250	$3.6 + f(T)$
R_{23}	$CO_2* + * \rightarrow CO* + O*$	4.18×10^{10}	0.177	$26.4 + f(\theta_O,\theta_{CO},T)$
R_{24}	$CO* + O* \rightarrow CO_2* + *$	2.39×10^{11}	−0.177	$20.6 + f(\theta_O,\theta_{CO},T)$
		Coupling Between CO and H₂ Chemistries on Pt		
R_{25}	$CO_2* + H* \rightarrow CO* + OH*$	8.03×10^{10} *8.03×10^8*	−0.531	$6.0 + f(\theta_O,\theta_H,\theta_{H_2O},\theta_{CO},T)$
R_{26}	$CO* + OH* \rightarrow CO_2* + H*$	1.25×10^{11} *1.25×10^9*	0.531	$18.5 + f(\theta_O,\theta_H,\theta_{H_2O},\theta_{CO},T)$
R_{27}	$COOH + * \rightarrow COOH*$	6.34×10^{-2}	−0.089	0.0
R_{28}	$COOH* \rightarrow COOH + *$	1.12×10^{13}	0.089	$55.3 + f(T)$
R_{29}	$COOH* + * \rightarrow CO* + OH*$	8.43×10^{10} *8.43×10^8*	0.024	$5.3 + f(\theta_O,\theta_{H_2O},\theta_{CO},T)$ $2.5,^b 5.5^c$
R_{30}	$CO* + OH* \rightarrow COOH* + *$	1.19×10^{11} *1.19×10^9*	−0.024	$19.1 + f(\theta_O,\theta_{H_2O},\theta_{CO},T)$ $22.1,^b 13.8^c$
R_{31}	$COOH* + * \rightarrow CO_2* + H*$	1.06×10^{11}	0.549	$1.0 + f(\theta_H,T)$ $1.0,^b \sim0.0^c$
R_{32}	$CO_2* + H* \rightarrow COOH* + *$	9.45×10^{10}	−0.549	$2.4 + f(\theta_H,T)$ $2.4,^b 14.3^c$
R_{33}	$CO* + H_2O* \rightarrow COOH* + H*$	1.10×10^{11}	0.492	$23.7 + f(\theta_H,\theta_{OH},\theta_{H_2O},\theta_{CO},T)$ $23.7,^d 28.1^e$
R_{34}	$COOH* + H* \rightarrow CO* + H_2O*$	9.07×10^{10}	−0.492	$5.6 + f(\theta_H,\theta_{OH},\theta_{H_2O},\theta_{CO},T)$
R_{35}	$CO_2* + OH* \rightarrow COOH* + O*$	5.35×10^{10}	0.097	$26.5 + f(\theta_O,\theta_{H_2O},T)$
R_{36}	$COOH* + O* \rightarrow CO_2* + OH*$	1.87×10^{11}	−0.097	$7.0 + f(\theta_O,\theta_{H_2O},T)$
R_{37}	$CO_2* + H_2O* \rightarrow COOH* + OH*$	8.64×10^{10}	−0.031	$17.5 + f(\theta_O,\theta_{OH},\theta_{H_2O},T)$
R_{38}	$COOH* + OH* \rightarrow CO_2* + H_2O*$	1.16×10^{11}	0.031	$11.9 + f(\theta_O,\theta_{OH},\theta_{H_2O},T)$ $11.9,^d 5.3^e$
R_{39}	$HCOO + 2* \rightarrow HCOO**$	1.46×10^{-1}	0.201	0.0
R_{40}	$HCOO** \rightarrow HCOO + 2*$	4.83×10^{12}	−0.201	$53.0 + f(T)$
R_{41}	$CO_2* + H* \rightarrow HCOO**$	1.12×10^{11}	−0.422	$18.5 + f(\theta_H,T)$
R_{42}	$HCOO** \rightarrow CO_2* + H*$	8.96×10^{10}	0.422	$0.0 + f(\theta_H,T)$
R_{43}	$CO_2* + OH* + * \rightarrow HCOO** + O*$	6.17×10^{10}	0.236	$36.8 + f(\theta_O,\theta_{H_2O},T)$
R_{44}	$HCOO** + O* \rightarrow CO_2* + OH* + *$	1.62×10^{11}	−0.236	$0.0 + f(\theta_O,\theta_{H_2O},T)$
R_{45}	$CO_2* + H_2O* + * \rightarrow HCOO** + OH*$	1.02×10^{11}	0.095	$25.8 + f(\theta_O,\theta_{OH},\theta_{H_2O},T)$
R_{46}	$HCOO** + OH* \rightarrow CO_2* + H_2O* + *$	9.78×10^{10}	−0.095	$3.0 + f(\theta_O,\theta_{OH},\theta_{H_2O},T)$

[a] Parameters of R_1−R_{18} correspond to the optimized, thermodynamically consistent mechanism of H₂ oxidation of the Appendix, those of CO oxidation (R_{19}−R_{24}) are from ref 19, and those of the coupling reactions R_{25}−R_{46} are unoptimized, but thermodynamically consistent. The activation energies are temperature dependent according to statistical mechanics (see Table 2). The modified Arrhenius expression

$$k = \frac{A}{\sigma^{n-1}} \left(\frac{T}{T_0}\right)^\beta e^{-E/RT} \text{ or } k = \frac{s}{\sigma^n} \sqrt{\frac{RT}{2\pi M}} \left(\frac{T}{T_0}\right)^\beta e^{-E/RT}$$

is used for computing the rate constant k. Here, A is the pre-exponential, s is the sticking coefficient, σ is the site density, n is the reaction order, β is the temperature exponent, E is the activation energy, R is the ideal gas constant, and T is the absolute temperature. The coverage dependence of the activation energies of various reaction steps is incorporated in our simulations on-the-fly via the UBI−QEP method. Functions f's in the last column represent such nonlinear dependence of activation energies on temperature and coverage. A bond index of 0.5 is used in the calculation of all activation energies reported here except for step R_{23}.[19] The backward activation energy (R_{24}) is calculated using the heat of reaction and the forward activation energy (R_{23}). Suggested pre-exponentials for R_9−R_{10}, R_{25}−R_{26}, and R_{29}−R_{30} that improve quantitative agreement with TPR experiments are shown in italics. [b] UBI−QEP-based activation energy at $\theta_{CO} = ^1/_6$, $\theta_{OH} = ^1/_3$, and $\theta_{H_2O} = ^1/_3$. [c] DFT-based activation energy reported in ref 18 within an H₂O* + OH* mixed phase ($\theta_{CO} = ^1/_6$, $\theta_{OH} = ^1/_3$, and $\theta_{H_2O} = ^1/_3$). [d] UBI-QEP-based activation energy at zero coverage. [e] DFT-based activation energy reported in refs 32−33 using cluster calculations (low coverages).
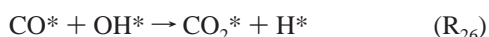
production is facilitated through the formation of the COOH* intermediate.

Pt is one of the better catalysts for CH_4 POX and CO PROX, but it is not as good for WGS. Nonetheless, any microkinetic model on Pt should be capable of describing all of these processes. In recent work, we focused on developing a thermodynamically consistent surface reaction mechanism for CO oxidation on Pt.[19] As we will illustrate, thermodynamic consistency of microkinetic models is essential, especially for WGS that can be equilibrium limited. As mentioned already, this issue can also be important downstream of the main reaction zone of POX. For this reason, in the Appendix of this paper, we extend the microkinetic model development to H_2 oxidation on Pt (see the Appendix for model development, optimization, thermodynamic consistency, and validation) as an essential building block of the CO−H_2 coupled reaction mechanism. The organization of this paper is as follows. The aforementioned TPR experiments and DFT calculations, which underscore the importance of coupling between the CO and H_2 reactions, are first discussed along with an assessment of the available microkinetic models. A H_2/CO/O_2 surface reaction mechanism with coupling reactions (i.e., reaction steps absent from the individual submechanisms) is then proposed to explore the importance of coupling reactions, such as the promoting role of H_2O in the low-temperature CO oxidation as well as in the WGS and PROX processes. To our knowledge, this is the only surface reaction mechanism that incorporates such coupling reactions and can serve as a building block for a comprehensive POX reaction mechanism of natural gas on transition metals.

Role of Water in the Catalytic Oxidation of CO

TPR Experiments of Bergald et al. Bergald et al.[17] studied the role of H_2O in the catalytic oxidation of CO at low temperatures using TPR experiments for three cases (different sets of initial coverages). Experimental data for the second and third cases are summarized in Figure 1. In the first experiment, 50% CO* and 25% O* were allowed to react. The normal CO_2 production peak was observed at ∼310 K. In the second experiment (referred to also as the annealing case), they explored the effect of OH* on the CO oxidation by first converting some of the preadsorbed H_2O* into OH* via annealing (some O* is also consumed in this process). H_2O molecules, which are not stabilized by the coadsorbates, desorb during annealing. In addition to the normal peak, a low-temperature CO_2 production peak was also observed at ∼200 K (see Figure 1a). In the third experiment (referred to also as the nonannealing case), 50% CO*, 25% O*, and 20% H_2O* were allowed to react without any prior surface annealing. Two CO_2 production peaks were again observed, as shown in Figure 1b, at similar locations as those in the annealing experiment.

On the basis of the lower-temperature CO oxidation peak, Bergald et al. concluded that adsorbed H_2O* promotes CO oxidation at low temperatures. In particular, they suggested that OH* plays an autocatalytic role in low-temperature CO oxidation, according to the following reactions
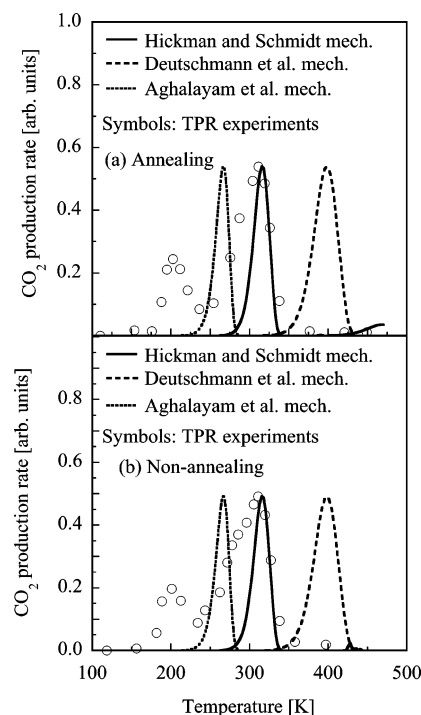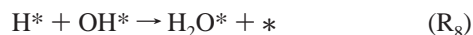
$$H_2O* + O* \rightarrow 2OH* \qquad (R_9)$$

$$CO* + OH* \rightarrow CO_2* + H* \qquad (R_{26})$$

$$H* + O* \rightarrow OH* + * \qquad (R_6)$$

or

$$H* + OH* \rightarrow H_2O* + * \qquad (R_8)$$

Figure 1. Comparison of the predictions using literature mechanisms[4,5,20] against the TPR experimental data of ref 17 for the annealing (panel a) and nonannealing (panel b) cases. The operating conditions include a pressure of 3×10^{-10} Torr, a ramp rate of 1 K/s, and an initial temperature of 128 K. The initial coverages are 50% CO*, 23% O*, and 4% OH* (it is assumed that 2% H_2O* reacts with 2% O* to produce 4% OH*) for the annealing case and 50% CO*, 25% O*, and 20% H_2O* for the nonannealing case. The literature mechanisms do not show any low-temperature activity.

DFT Studies of Gong and Hu. Motivated by the experiments of Bergald et al.,[17] Gong and Hu[18] carried out periodic slab DFT calculations to explore the reaction energetics of low-temperature CO oxidation. They observed that the CO* + O* oxidation barrier is reduced in the presence of H_2O* because of hydrogen bonding between the H of H_2O* and the transition state. However, they further suggested that, under the operating conditions of the TPR experiments, the probability of this reaction is very low compared to the faster reaction between H_2O* and O* or the fast H_2O* desorption. Also, the reaction between CO*, O*, and H_2O* would be a trimolecular one and, therefore, less probable. Given these issues, Gong and Hu proposed essentially the same autocatalytic mechanism as that of Bergald et al., with the additional possibility of the carboxyl (COOH*) intermediate formation. COOH* can transfer an H to an adjacent H_2O*, and at the same time, an H in H_2O* is transferred to an adjacent OH* to produce CO_2* and H_2O*. This reaction could be represented in a single step as

$$COOH* + H_2O* + OH* \leftrightarrow CO_2* + 2H_2O* \qquad (2)$$
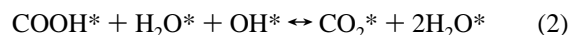
Considering all these proposed hypotheses, it is important to explore the low-temperature CO oxidation with a microkinetic model that couples the CO and H_2 chemistries, including formation and decomposition pathways of the oxygenates. Before we investigate this, we will first compare the performance of the existing literature mechanisms against the experiments of Bergald et al.[17] to illustrate the importance of the coupling reaction steps.

Performance of Available Literature Mechanisms. Surface reaction mechanisms for CH_4 oxidation on Pt have been

Microkinetic Modeling for CO Oxidation

J. Phys. Chem. B, Vol. 108, No. 39, 2004 **15249**

proposed by several groups, including Hickman and Schmidt,[4] Deutschmann et al.,[5] Frauhammer and Veser,[7] and Aghalayam et al.[20] The experiments of Bergald et al.[17] are modeled using three of these reaction schemes, and the comparison is shown in Figure 1 for the annealing and nonannealing cases. The stiff system of differential/algebraic equations is solved using the *DDASSL* solver.[21] For the annealing case, it is assumed that 2% H_2O^* reacts with 2% O^* to produce 4% OH^*. Therefore, the initial coverages are taken to be 50% CO^*, 23% O^*, and 4% OH^* (we will return to the initial coverage of OH^* in a later section).

As shown in Figure 1, the three reaction mechanisms predict a single CO_2 production peak (at ~316, ~398, and ~267 K using the Hickman and Schmidt, Deutschmann et al., and Aghalayam et al. mechanisms, respectively) for both experiments. Because of a lack of coupling between the CO and H_2 chemistries in the first two mechanisms, they are unable to capture the low-temperature CO oxidation. In the mechanism by Aghalayam et al., the activation energies of the $CO^* + O^*$ (3.6 kcal/mol) and $CO^* + OH^*$ (8.4 kcal/mol) reactions are small, whereas that of the CO_2 desorption is large (17 kcal/ mol). Thus, even though the coupling reaction, $CO^* + OH^* \leftrightarrow CO_2^* + H^*$, was included, the CO_2 production is limited by the CO_2^* desorption, and only one peak is observed. Furthermore, these mechanisms are thermodynamically inconsistent, as further discussed in the WGS section. Next, we propose a thermodynamically consistent surface reaction mechanism that also accounts for the $CO-H_2$ coupling.

A Surface Reaction Mechanism for Coupled $CO-H_2$ Reactions On Pt

A surface reaction mechanism composed of three submechanisms (H_2 oxidation, CO oxidation, and $CO-H_2$ coupling steps) is shown in Table 1. The development, optimization, and validation of the H_2 oxidation mechanism (steps R_1-R_{18}) are elaborated in the Appendix. The steps of the CO oxidation mechanism ($R_{19}-R_{24}$) are taken from ref 19. The additional coupling steps ($R_{25}-R_{46}$) are proposed here to account for different possibilities of coupling. The heats of chemisorption of all species are listed in Table 2 and are typically based on average literature values of heats of chemisorption on single crystals and polycrystalline catalysts. Those of $COOH^*$ and $HCOO^{**}$ are taken from ref 22 (a comparable value of 53.9 kcal/mol was also reported by Gong and Hu[18] for $COOH^*$). Activation energies of all reactions are calculated using the unity bond index quadratic exponential potential (UBI−QEP)[23,24] method. The function f' in the last column of Table 1 indicates that the activation energies are coverage and temperature dependent. The former dependence arises from the variation of heats of chemisorption with coverages. The latter is built in using statistical mechanics. These functions are obtained in our simulations on-the-fly using the UBI−QEP method.[23,24] Details of the approach followed to obtain the functions f', and examples are also given in refs 11 and 25. The individual mechanisms for H_2 and CO oxidation are made thermodynamically consistent through optimization of pre-exponentials, starting from nominal transition-state-theory (TST)-based values[26] against experiments and gas-phase thermodynamics (see the Appendix and ref 11 for the optimization approach). The pre-exponentials of the coupling reactions ($R_{25}-R_{46}$) are made thermodynamically consistent around TST values based on gas-phase thermodynamics only (but not against any experiments) (i.e., by reducing the distance between the entropies of gas-phase and surface reactions) following the approach of ref 11. Suggested values for some of these pre-exponentials are discussed in a later section.

TABLE 2: Temperature- and Coverage-Dependent Heats of Chemisorption Using Statistical Mechanics and the UBI−QEP Method[11,19], ^{a}

species	heat of chemisorption Q (kcal/mole)	temperature dependence^b $[Q(T_0) - Q(T)]/R\Delta T$	changes in degrees of freedom to derive the temperature dependence^c
O^*	$85 - 16\theta_O$	1.5	$-3F_T + 3F_V$
H^*	$62 - 3\theta_H$	1.5	$-3F_T + 3F_V$
OH^*	$63 - 33\theta_O + 25\theta_{H_2O}$	2.0	$-3F_T - 2F_R + F_{RR} + 4F_V$
H_2O^*	$10 - 2.5\theta_{H_2O} + 25\theta_{OH}$	2.5	$-3F_T - 3F_R + F_{RR} + 5F_V$
CO^*	$40 - 15\theta_{CO}$	2.0	$-3F_T - 2F_R + F_{RR} + 4F_V$
CO_2^*	3.6	2.0	$-F_T - 3F_R + 4F_V$
$COOH^*$ (C bonded to Pt)	55.3	2.5	$-3F_T - 3F_R + F_{RR} + 5F_V$
$HCOO^{**}$ (both oxygens bonded to Pt, i.e., a bidentate)	53.0	3.0	$-3F_T - 3F_R + 6F_V$

^{a} Heat of chemisorption, $Q(T)$, decreases with increasing temperature (here, $\Delta T = T - T_0$ and $T_0 = 300$ K). The heats of chemisorption for $COOH^*$ and $HCOO^{**}$ are taken from DFT calculations from ref 22, and the rest are taken from refs 8 and 19. For the coverage effects in the heats of chemisorption, refer to refs 8 and 19 and the text. The gas phase thermodynamic data is taken from ref 46 and the data for COOH and HCOO from ref 48. ^{b} The generalized assumptions to calculate the temperature dependence are as follows: (1) Each translational, rotational, and vibrational degree of freedom (DF) corresponds to $0.5RT$, $0.5RT$, and RT, respectively. (2) Upon adsorption, all translational DF are converted into vibrational DF. In the case of weakly bound molecules (such as CO_2), only 1 translational DF is lost upon adsorption (the molecule is able to move readily on the surface). (3) All rotational DF are converted into vibrational DF upon adsorption. For species such as OH^*, H_2O^*, and $COOH^*$ with a vertical axis through the adsorbed atom, one of the gained vibrational DF is assumed to be a free, internal rotor (rigid rotor approximation) and counts as $0.5RT$. ^{c} F_T, F_R, and F_V stand for translational, rotational, and vibrational DF. F_{RR} indicates that a vibrational DF is assumed to be a free, internal rotor. The minus and plus signs indicate loss and gain of DF, respectively.

Exploring Different Pathways of Coupling in the H_2O-Promoted Oxidation of CO

The $CO-H_2$ mechanism, consisting of steps R_1-R_{24}, is the basis of most microkinetic models of methane POX. In this basic mechanism, coupling between the H_2 and CO reactions occurs by site competition and sharing of the oxidant, O^*. Another example of possible coupling entails the formation of O^* from the dissociation of H_2O^* and its subsequent reaction with CO^* (i.e., $CO^* + O^* \rightarrow CO_2^* + *$). However, in the next section, this coupling is shown to be insufficient to explain various experimental features.

The Basic CO and H_2 Reaction Sets Against the TPR CO Oxidation Data. The H_2 and CO oxidation mechanisms have been validated individually (see the Appendix and ref 19, respectively). The basic $CO-H_2$ mechanism (R_1-R_{24}) without any other coupling reactions is assessed against the TPR experiments of Bergald et al.[17] In the first experiment with 50% CO and 25% O, the mechanism shows a high-temperature peak at ~283 K, in reasonable agreement with the experimental data (not shown). Figure 2 compares our simulations and the experimental data for the annealing and nonannealing experiments. The high-temperature CO_2 production peak is reasonably captured by our basic mechanism in both cases. However, this mechanism does not show any low-temperature peak for either experiment, because of the absence of coupling reactions between the CO and H_2 chemistries. In addition to the usual peak at ~283 K, some high-temperature activity at ~431 K is observed from OH^* decomposition (with a high activation
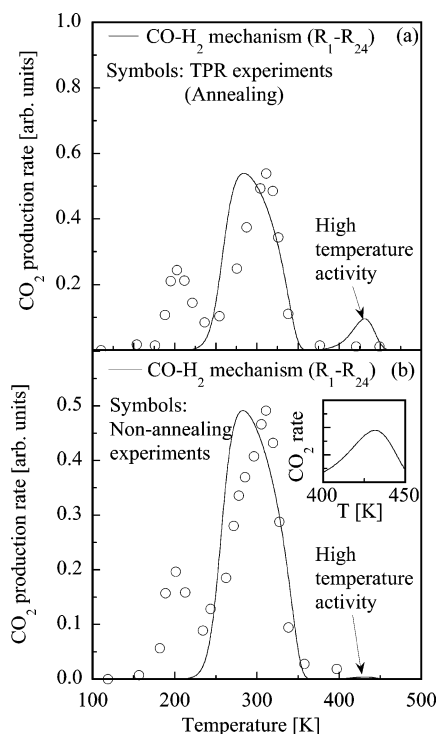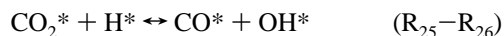
Figure 2. Comparison of the predictions of the basic $CO-H_2$ mechanism (R_1-R_{24}) against the TPR experimental data of ref 17 for the annealing (panel a) and nonannealing (panel b) cases. The operating conditions are the same as in Figure 1. In the absence of coupling reactions, the basic mechanism does not show any low-temperature activity but exhibits high-temperature activity, in contrast to the experiments. The inset in panel b magnifies the high-temperature activity.

energy of ~27 kcal/mol) followed by the CO* + O* reaction. However, this feature is inconsistent with the experimental data.

Direct CO$_2$ Production Pathway. Next, we include the reversible coupling reaction (hereafter called the direct pathway to CO$_2$)

$$CO_2^* + H^* \leftrightarrow CO^* + OH^* \qquad (R_{25}-R_{26})$$

proposed in ref 20. Figure 3 shows the predictions of the CO−H$_2$ mechanism with this direct pathway (−) added to the basic CO−H$_2$ mechanism (R_1-R_{24}) for the second TPR experiment[17] (i.e., the annealing case with a small fraction of OH* (4%) present on the catalyst surface along with 50% CO* and 23% O*). Figure 4 shows the coverage of selected species. As shown in Figure 4a, in the presence of OH*, CO* + OH* produces CO$_2$* and H* at ~174 K. CO$_2$ desorbs immediately because of a very low chemisorption energy, whereas H* reacts with O* to replenish OH*. The reaction between H* and OH* competes with that between CO* and OH*, and H$_2$O* formation is observed, which then desorbs at ~184 K, as shown in Figure 3b. The continuous production of OH* through R$_6$ (H* + O* → OH* + *) and the consumption through R$_{26}$ (CO* + OH* → CO$_2$* + H*) result in an autocatalytic effect of OH* on CO oxidation, manifested by low-temperature activity in the temperature range ~180−230 K, even after the low-temperature peak. At high temperatures, the only dominant species on the surface are CO* and O*, as shown in Figure 4a, which react to produce the usual CO$_2$ peak at ~293 K.

Our assumption of 4% initial OH* coverage is arbitrary and has been explored by performing simulations for different initial OH* coverages. The results are summarized in Figure 5. Two CO$_2$ production peaks are observed for all initial OH* coverages
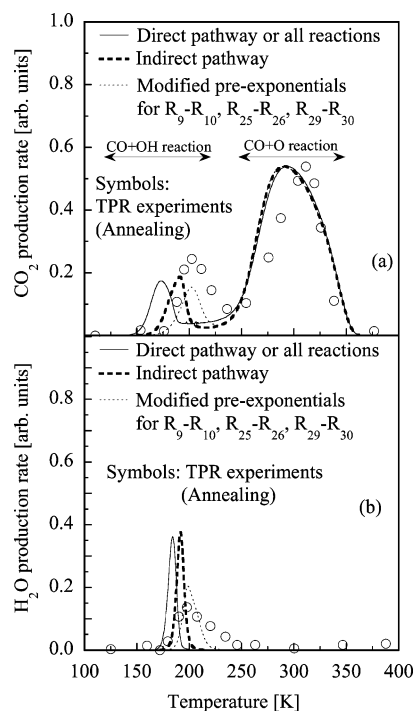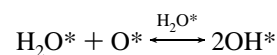

Figure 3. Comparison of the predicted CO$_2$ and H$_2$O production rates using the proposed CO−H$_2$ mechanism with either the direct (−, steps R_1-R_{24} plus $R_{25}-R_{26}$) or the indirect (- - -, steps R_1-R_{24} plus $R_{27}-R_{32}$) CO$_2$ formation pathways against the TPR experimental data of ref 17 for the annealing case. The operating conditions are the same as in Figure 1. The initial coverages are 50% CO*, 23% O*, and 4% OH*. In the presence of OH*, the coupling chemistry can capture both the low- and high-temperature CO oxidation peaks observed in the experiments. The full mechanism (R_1-R_{46}) gives basically the same predictions as that of R_1-R_{24} with the direct pathway, $R_{25}-R_{26}$, added. Predictions with modified pre-exponentials for R_9-R_{10} (multiplied by 10), $R_{25}-R_{26}$ (divided by 100), and $R_{29}-R_{30}$ (divided by 100) are also shown. The low-temperature peaks for CO$_2$ and H$_2$O production shift toward the experimental ones. Furthermore, the width of the H$_2$O peak is in better agreement with the experiments using these modified pre-exponentials.

studied, but the relative magnitude of the first peak depends on the initial fraction of OH* (i.e., on the annealing process). In fact, an initial OH* coverage of 6% shows better agreement with the published annealing experiments. Therefore, our assumption of 4% initial OH* appears reasonable. Given the uncertainty in the initial conditions, we do not attempt to fine-tune the reaction pre-exponentials to better match the simulations with the experimental peak heights.

Figure 6 shows the TPR experimental data and simulations for initial coverages of 50% CO*, 25% O*, and 20% H$_2$O* corresponding to the third TPR experiment (i.e., the nonannealing case). Our simulations show the low-temperature reactivity observed experimentally, but the magnitude is much smaller. As shown in the inset of Figure 6b, a small fraction of H$_2$O* undergoes disproportionation with O* to produce OH*. OH* subsequently reacts with CO* at ~183 K to produce CO$_2$* and H*. The pathways are essentially the same as in the case of annealing. The increase in OH stability due to hydrogen bonding (see the Appendix and Table 2 for coverage-dependent heats of chemisorption) between H$_2$O* and OH* is responsible for the decrease in the activation energy of the disproportionation step R$_9$

$$H_2O^* + O^* \xrightarrow{H_2O^*} 2OH^*$$

and, hence, for the low-temperature peak. When the hydrogen-

Microkinetic Modeling for CO Oxidation

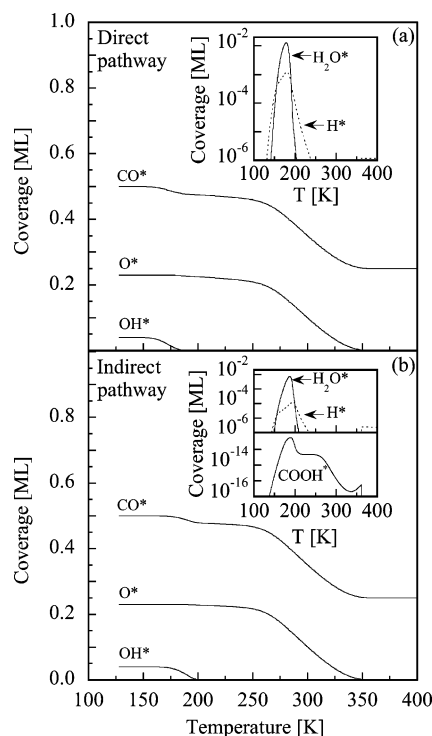*J. Phys. Chem. B, Vol. 108, No. 39, 2004* **15251**

Figure 4. Dominant coverages in the annealing experiment using the direct pathway (panel a) and the indirect pathway (panel b) for the conditions of Figure 3. The insets show the H_2O^*, H^*, and $COOH^*$ coverages.
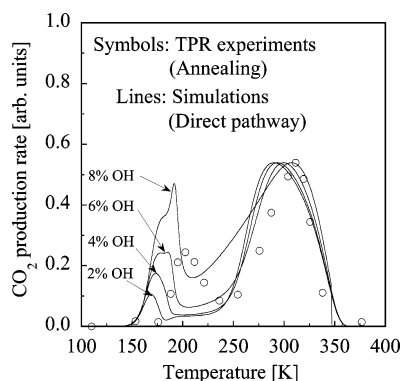

Figure 5. Effect of initial OH^* coverage on TPR in the annealing experiment. The basic $CO-H_2$ mechanism with the direct CO_2 formation pathway is used. The operating conditions are the same as in Figure 1. The initial coverages are 50% CO^*, $(25 - x/2)$% O^*, and x% OH^*. Two peaks are observed for all OH^* coverages studied.

bonding interactions are eliminated from the mechanism, no low-temperature activity is observed. Again, the autocatalytic effect of OH^* through steps R_6 ($H^* + O^* \rightarrow OH^* + *$) and R_{26} ($CO^* + OH^* \rightarrow CO_2^* + H^*$) gives rise to the low-temperature CO_2 production activity in the temperature range ~180–230 K after the low-temperature peak.

These simulations indicate the significance of the $CO-OH$ coupling reactions in a microkinetic model. Yet, the agreement between simulations and experiments is not spectacular. The low-temperature peaks in annealing and nonannealing cases occur at slightly lower temperatures than the experimental ones (by ~30 and ~18 °C). Furthermore, the width of the H_2O production peak in Figure 3b is narrower than the experimental one. Our simulations show a low-temperature CO_2 peak in the nonannealing case, but its intensity is small compared to the experiments. The lack of quantitative agreement may in part be due to the formation of a carboxyl ($COOH^*$) intermediate,
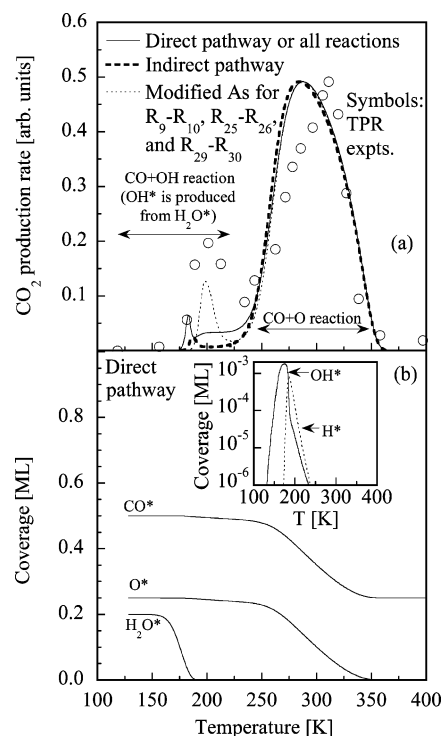

Figure 6. Predicted CO_2 production rate and corresponding dominant surface coverages using the basic $CO-H_2$ mechanism with direct and indirect CO_2 formation pathways against the TPR experimental data of ref 17 for the nonannealing case. The operating conditions are the same as in Figure 1. The initial coverages are 50% CO^*, 25% O^*, and 20% H_2O^*. In the presence of H_2O^*, the hydrogen bonding between H_2O^* and OH^* (see Appendix) as well as the coupling chemistry play an essential role in creating the low-temperature peak. The full mechanism (R_1-R_{46}) gives the same predictions as that of R_1-R_{24} with the direct pathway, $R_{25}-R_{26}$, added. Predictions with modified pre-exponentials for R_9-R_{10} (multiplied by 10), $R_{25}-R_{26}$ (divided by 100), and $R_{29}-R_{30}$ (divided by 100) are also shown. The low-temperature CO_2 production peak and the height are in better agreement with the experiments.

as suggested by Bergald et al.[17] and Gong and Hu,[18] and in part to the uncertainties in the parameters of the reaction mechanism. We will explore both possibilities.

An Indirect CO_2 Formation Pathway: The Role of Carboxyl. In addition to the basic mechanism (R_1-R_{24}), here, we consider the steps $R_{27}-R_{32}$. We call this the indirect pathway of CO to CO_2 formation, because it goes through the intermediate $COOH^*$. The adsorption/desorption of COOH is also included (even though it is unimportant). It should be noted that the reaction steps $R_{25}-R_{26}$ (direct pathway) are left out of the following analysis.

TPR simulations are again carried out to understand the effect of these steps. Figure 3a (- - -) shows that the low-temperature CO_2 production peak in the annealing case is shifted by ~17 °C toward the actual experimental peak. A similar shift of ~4 °C toward the actual experimental peak is observed in the nonannealing case, as shown in Figure 6a (- - -). The slightly higher activation energy of R_{30} ($CO^* + OH^* \rightarrow COOH^* + *$) compared to that of R_{26} ($CO^* + OH^* \rightarrow CO_2^* + H^*$) is responsible for such a shift. From these results, it is evident that carboxyl chemistry could also explain the low-temperature CO oxidation peak, depending on the relative selectivities of the direct and indirect pathways.

The Relative Importance of Various CO_2 Formation Pathways. Upon adding both the direct and indirect pathways ($R_{25}-R_{32}$) to the basic mechanism (R_1-R_{24}), it is observed that

the low-temperature peak location in the annealing case is again at ~174 K, indicating that the direct pathway is dominant in this particular experiment. Reaction path analysis (RPA) shows that the selectivity of the direct pathway is ~94% (and that of the indirect pathway is ~6%) at the low-temperature peak. If the pre-exponentials of both the direct and indirect pathways (R_{25}–R_{26} and R_{29}–R_{32}) are decreased by a factor of 100, the simulated low-temperature peak shifts to the experimental one, as shown in Figure 3a. The selectivities of the direct and indirect paths at the peak temperature become ~90% and ~10%, respectively. If the pre-exponentials of only the direct pathway are decreased by a factor of 10 (or 100), the selectivity to the indirect pathway increases to ~47% (~90%). Calculations for the nonannealing case show similar behavior. Note that when these changes in pre-exponentials are carried out, the equilibrium constants are kept fixed, so thermodynamic consistency is maintained. Step R_{33}

$$CO^* + H_2O^* \rightarrow COOH^* + H^* \qquad (R_{33})$$

is also an indirect pathway to CO_2 formation. However, RPA indicates that R_{33} is not important under the TPR conditions because of fast H_2O desorption in the nonannealing case. At this stage, it is not clear whether R_{33} is an elementary step, but its inclusion does not alter the main conclusions of this work.

Overall, our simulations indicate that the selectivities of the direct and indirect pathways are within an order of magnitude or less. Because the energetics in our mechanism are based on the semiempirical UBI–QEP method, and the pre-exponentials for the coupling steps are not optimized against any experiments, it is not possible at this stage to assertively distinguish between the different pathways in actual experiments. Additional reactions involving $COOH^*$ and $HCOO^{**}$ (R_{33}–R_{46}) with thermodynamically consistent rate parameters are not important for these particular experiments. Even though the heats of chemisorption of COOH and HCOO are similar, the unimportance of the formate path compared to the carboxyl one is mainly due to the significantly different gas-phase heats of reaction involving these species that make the formation of $HCOO^{**}$ activated (R_{41}, $CO_2^* + H^* \rightarrow HCOO^{**}$) and less probable. Furthermore, CO_2 preferentially desorbs rather than reacts because of its low chemisorption energy.

Regarding previously published hypotheses, RPA shows that the probability of the $CO^* + O^*$ reaction at low temperatures in the presence of H_2O^* is negligible, in agreement with the suggestion of ref 18. Furthermore, there is no low-temperature activity in the absence of coupling reactions (i.e., the direct pathway $CO^* + O^*$ is ineffective). Our simulations indicate that most of the H_2O^* desorbs and some undergoes disproportionation with O^* at low temperature as suggested by Gong and Hu.[18] Finally, on the basis of RPA, the hypothesis of Gong and Hu that the $COOH^*$ can transfer an H to OH^* through H_2O (see eq 2) looks improbable.

Effect of Kinetic Parameters on TPR Predictions. The inclusion of the indirect CO_2 formation path can also explain the experimental features (low CO oxidation peak), but quantitative agreement between simulations and experiments is still lacking. Given the uncertainty of DFT or UBI–QEP calculations and experimental measurements and the fact that pre-exponentials of coupling reactions are made thermodynamically consistent but are unoptimized, it is worth exploring the effect of kinetic parameters on model predictions. Reaction path analysis and sensitivity analysis (SA) are ideal tools for doing this. Overall, the agreement can be improved with reasonable (and
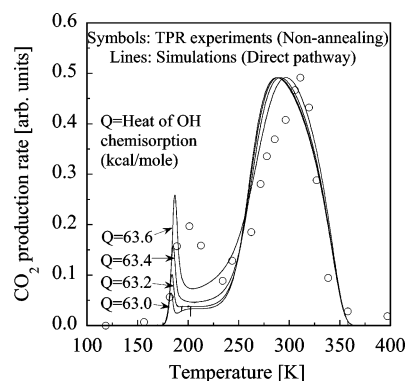

Figure 7. Effect of the heat of OH chemisorption (Q) on the TPR spectra in the nonannealing experiment using the basic CO–H_2 mechanism with the direct CO_2 formation pathway. The operating conditions are the same as in Figure 1b. The initial coverages are 50% CO*, 25% O*, and 20% H_2O^*. A slight increase (~0.6 kcal/mol) in Q is sufficient to capture the height of the low-temperature peak.

in some cases small) changes in kinetic parameters. A summary of such changes and results will be given next.

The difference in the CO_2 peak position in the annealing experiment can be eliminated by a small increase in the activation energies of R_{26} ($CO^* + OH^* \rightarrow CO_2^* + H^*$) and R_{30} ($CO^* + OH^* \rightarrow COOH^* + *$) by ~1.8 kcal/mol or a more drastic decrease in the pre-exponentials of R_{25}–R_{26} and R_{29}–R_{30} by a factor of ~100. Figure 3a shows the improved predictions. Such a change in the pre-exponentials can also better capture the height and width of the H_2O production peak, as shown in Figure 3b.

As another example, Figure 7 shows the effect of the heat of OH chemisorption on the predictions for the nonannealing case. It is observed that a slight increase by ~0.6 kcal/mol in the heat of OH chemisorption can result in a peak height of low-temperature CO_2 production that is comparable to the experimental data. Alternatively, if the pre-exponentials of R_{25}–R_{26} and R_{29}–R_{30} are decreased by a factor of ~100 and those of R_9–R_{10} are increased by a factor of ~10, the height and location of the low-temperature CO_2 production peak is better captured for the nonannealing case, as shown in Figure 6a. Reaction path analysis at low temperatures (~160 K) shows that, after modifying these pre-exponentials, the relative importance of H_2O^* disproportionation compared to H_2O^* desorption increases from ~3% to ~31%. The increased rate of R_9 produces more OH^*, which in turn can more effectively oxidize CO*.

Modified pre-exponentials that improve the agreement between model predictions and experimental data are indicated in Table 1 in italics. These modified pre-exponentials have no effect on the predictions of the optimized H_2 mechanism presented in the Appendix. A combination of slight changes in heats of chemisorption and pre-exponentials is expected to give even better agreement, but we leave this task out of this work because the uncertainties are such that a unique set of parameters cannot be obtained. Overall, a slight change in energetics (well within the uncertainty of UBI–QEP or DFT) is adequate to explain the low-temperature experimental data and should be preferred, whereas more drastic changes in pre-exponentials appear to be necessary to do a similar job.

Role of Coupling Reactions in WGS and PROX Reactions

Water–Gas Shift Reaction. The WGS reactor is an essential part of the H_2 production process for fuel cells. This reaction is also important from a modeling point of view because of the
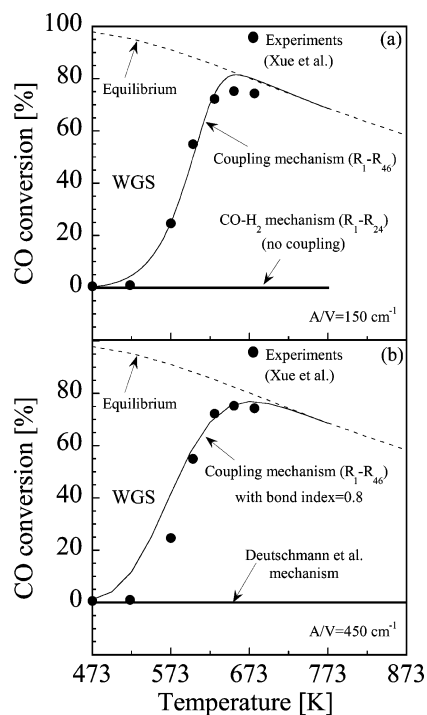
Microkinetic Modeling for CO Oxidation

J. Phys. Chem. B, Vol. 108, No. 39, 2004 **15253**

Figure 8. Comparison of the predictions of the basic CO−H₂ mechanism (R₁−R₂₄) and full mechanism (R₁−R₄₆) against the WGS experimental data of ref 27. In panel a, the bond index of all coupling reactions is 0.5, whereas in panel b, it is 0.5 for all coupling reactions except for R₂₅−R₂₆ and R₂₉−R₃₀, where a value of 0.8 is used. The operating conditions are a pressure of 1 atm, an inlet flow rate of 50 cm³/min at STP (note that the inlet velocity changes with temperature), and an inlet composition of 5% H₂, 15% CO, 20% H₂O, 5% CO₂, and 55% N₂. The full thermodynamically consistent mechanism predicts the WGS data well in both the kinetically controlled and equilibrium-limited regimes. The coupling reactions are essential to give the necessary speed of the overall reaction. Predictions using the Deutschmann et al. mechanism[5] are also shown in panel b. The mechanism is thermodynamically inconsistent and does not show the "correct" speed because of a lack of coupling.

coupling between CO and H₂ chemistries and the fact that, at high temperatures, the process is equilibrium limited. As a result, any thermodynamically inconsistent mechanisms may fail in describing this process, irrespective of the catalyst. Xue et al.[27] carried out experiments in a tubular, fixed-bed reactor to measure the CO conversion as a function of temperature for typical WGS conditions on Pt/ZrO₂. The feed in these experiments was 5% H₂, 15% CO, 20% H₂O, 5% CO₂, and 55% N₂. The experimental data are shown in Figure 8a. Equilibrium calculations using *GASEQ* software[28] show that the experimental conversion of CO is well below equilibrium conversion at lower temperatures and approaches equilibrium conversion at higher temperatures (i.e., the experiments are kinetically controlled at low temperatures and thermodynamically controlled at high temperatures, as expected).

We simulated these experiments using a catalytic PFR model. External mass transfer is not important under these conditions. Furthermore, the Weisz criterion shows that internal mass transfer can also be neglected. As an example of the performance of the literature mechanisms, Figure 8b shows the predictions using the Deutschmann et al. mechanism.[5] This mechanism does not have the "correct" speed because of a lack of coupling reactions (see text to follow). Furthermore, the mechanism is thermodynamically inconsistent, because it shows ~100% conversion using a very high A/V (area of catalyst per unit volume of reactor) and a very long reactor.

Figure 8a shows the predictions using the basic CO−H₂ mechanism (R₁−R₂₄) without coupling reactions and with the coupling reactions (R₁−R₄₆). In the absence of the coupling reactions, the predicted CO conversion is almost zero despite our mechanism being thermodynamically consistent. By using an unrealistically long reactor and a large surface-to-volume ratio, equilibrium conversion at high temperatures can be reached. Upon inclusion of the coupling chemistry, the mechanism correctly predicts the trend in CO conversion. The only adjustable parameter here is the A/V that was not reported. (This value is associated with the assumed density of sites, i.e., the catalyst particle size and the dispersion of catalyst, and whether pre-exponentials have been optimized or not. In the absence of detailed catalyst particle information, A/V was set to 150 cm⁻¹ with a site density of 1.5 × 10¹⁵ sites/cm²).

RPA for the key intermediate OH* shows that the H₂O* decomposition to OH* + H* is fast (almost 100% OH* is produced from H₂O* decomposition), but the subsequent OH* decomposition to O* is negligible because of high activation energy. Therefore, the net CO* + O* reaction is slow, resulting in very low CO conversion. These simulations clearly indicate that, even at high temperatures, the coupling chemistry is essential to provide the "correct" speed of the overall WGS reaction, so equilibrium is approached at reasonable reactor lengths.

The most important reaction steps in controlling the model response in our full mechanism are R₂₅−R₂₆ and R₂₉−R₃₄. Upon inclusion of the coupling steps (R₂₅−R₄₆), RPA shows that the relative consumption of OH* through the direct and indirect pathways (R₂₆ + R₃₀) is significant (~100% at 473 K, ~62% at 623 K, but decreases at higher temperatures) compared to R₈, thus increasing the speed of CO₂ formation. Furthermore, the relative contribution of the indirect pathway (R₃₀) increases compared to the direct pathway (R₂₆) with increasing temperature (~37% at 473 K, ~45% at 623 K, and remains roughly the same at higher temperatures). This is due to the slightly higher activation energy of R₃₀ (CO* + OH* → COOH* + *) compared to that of R₂₆ (CO* + OH* → CO₂* + H*). RPA on CO* provides insight into the relative importance of the CO oxidation pathways. CO* is consumed via reactions R₂₄ (CO* + O* → CO₂* + *), R₂₆, R₃₀, and R₃₃ (CO* + H₂O* → COOH* + H*). A comparison of the relative rates of these reactions shows that the contribution of R₂₄ is negligible at all temperatures. Reactions R₃₀ and R₃₃ (indirect pathways via carboxyl intermediate) together dominate at low temperatures (e.g., ~99% contribution to CO oxidation at 473 K of very low conversion) but become comparable to the direct pathway (R₂₆) at higher temperatures (e.g., ~49% contribution to CO oxidation at 698 K), which are of practical interest. In comparing the indirect paths, reaction R₃₃ dominates over R₃₀ at lower temperatures but becomes less important at higher temperatures where the conversion is higher. Simulations with the modified pre-exponentials for R₉−R₁₀, R₂₅−R₂₆, and R₂₉−R₃₀ also show similar behavior as shown in Figure 8a and capture the experimental data with an A/V of ~475 cm⁻¹.

Preferential Oxidation of CO. PROX is another important process in H₂ production that reduces the harmful CO concentration for the catalysts of fuel cells. Here, we present a comparison of our simulations with the PROX experiments of Kahlich et al.[29] These researchers conducted integral flow measurements in a microreactor and estimated the CO conversion and selectivity to CO oxidation with a feed consisting of 1% CO, 1% O₂, 75% H₂, and 23% N₂. Figure 9a shows the
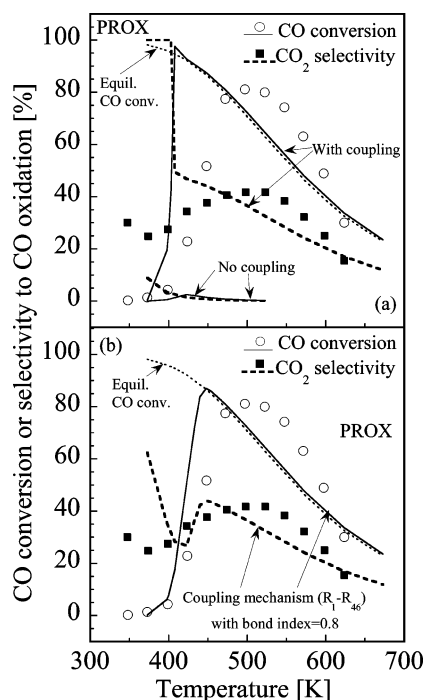
Figure 9. Comparison of the predictions of the basic $CO-H_2$ mechanism (R_1-R_{24}) and full mechanism (R_1-R_{46}) against the PROX experimental data of ref 29 for bond indices described in Figure 8. The equilibrium conversion of CO is also shown by a dotted line. The operating conditions are a pressure of 1 atm, a catalyst area of 10^5 cm^2, a reactor volume of $\sim$0.13 cm^3, an inlet flow rate of 120 nml/min (note that the inlet velocity changes with temperature), and an inlet composition of 1% CO, 1% O_2, 75% H_2, and 23% N_2. Small changes in energetics strongly affect the CO selectivity at very low CO conversions.

experimental data. The selectivity to CO oxidation was defined as

$$S = 0.5 \times \frac{[CO_2]^{out} - [CO_2]^{in}}{[O_2]^{in} - [O_2]^{out}} \qquad (3)$$

A PFR model was employed to simulate these experiments. External and internal mass transfer is found to be unimportant. Figure 9a shows the predictions of the basic $CO-H_2$ mechanism (R_1-R_{24}) without coupling reactions and with the full mechanism (R_1-R_{46}). The predicted CO conversion and selectivity to CO oxidation are very low when using the basic $CO-H_2$ mechanism, because of the lack of any coupling reactions. RPA for the key intermediates O* and OH* shows that O* is readily produced from dissociative O_2 adsorption ($\sim$100%) at lower temperatures and from OH* decomposition (>90%) at higher temperatures, but it is primarily consumed in OH* formation (>90% at all temperatures) through R_6. Almost all OH* is subsequently utilized in H_2O* formation ($\sim$100%) through R_8. As a result, the net CO* + O* reaction is slow, and the CO conversion as well as the selectivity to CO oxidation are low.

With the full mechanism (R_1-R_{46}), the rate of CO PROX is increased primarily because of reactions $R_{25}-R_{26}$ and $R_{29}-R_{34}$. RPA for the key intermediate OH* shows that, with increasing temperature, the percentage consumption of OH* through the direct and indirect pathways ($R_{26} + R_{30}$) decreases in favor of H_2O* formation via R_8 ($\sim$100% at 373 K, $\sim$74% at 498 K, and $\sim$8% at 673 K). The selectivity of the direct path (R_{26}) is slightly higher than that of the indirect path (R_{30}) but becomes comparable to it at higher temperatures. The net decrease in

the selectivity of ($R_{26} + R_{30}$) compared to R_8 (H* + OH* → H_2O* + *) results in a decrease in the selectivity to CO oxidation. The predicted CO conversion goes through a maximum as observed in the experiments, but ignition occurs earlier than in the experiments. The predicted selectivity to CO oxidation drops sharply with increasing temperature, whereas the experiments show a moderate change. Overall, our mechanism is highly selective ($\sim$100%) to CO oxidation at low temperatures, a feature not observed in the experiments. Possible reasons for these differences are discussed in the next section. Comparison of the rates of CO-consuming reactions R_{24}, R_{26}, R_{30}, and R_{33} shows that the contribution of R_{24} is low at low temperatures ($\sim$9% at 373 K of very low conversion) and becomes negligible as the temperature increases. The contribution of other CO-consuming reactions is non-monotonic. The indirect pathways R_{30} and R_{33} together dominate at higher conversions ($\sim$83% at 423 K) but are less important at lower conversions ($\sim$31% at 373 K and $\sim$58% at 673 K) compared to the direct pathway (R_{26}). R_{33} is the dominant carboxyl-forming path at intermediate temperatures. The rates of R_{26} and R_{30} are comparable, with the direct pathway (R_{26}) being slightly faster. Simulations with the modified pre-exponentials for R_9-R_{10}, $R_{25}-R_{26}$, and $R_{29}-R_{30}$ show similar behavior as shown in Figure 9a. The differences in selectivity at low temperatures, where the conversion is nearly zero, are of less concern, because the uncertainties in both experiments and simulations are large. In an attempt to explore the differences between simulations and experiments, we will elaborate on the simulation uncertainty next.

The equilibrium conversion is also shown in Figure 9. Note that the experimental CO conversion data are slightly higher than the equilibrium-predicted data, between 450 and 600 K, possibly because no methanation reactions were included in our equilibrium calculations. When methane is also included as a possible product, the predicted equilibrium conversion is higher than the experimental one (data not shown). Future work is needed to address the kinetic and equilibrium aspects of methanation.

Effect of Activation Energies of CO + OH Reactions on PROX and WGS Reactions. Given the uncertainty in predicting the activation energies as well as the possible differences between single crystals and polycrystalline catalysts (we typically consider average literature values of heats of chemisorption on single crystals and polycrystalline catalysts), here, we address the effect of activation energies of the CO + OH reactions on the WGS and PROX reactions. There are different ways to do this. One method includes changes in heats of chemisorption (see Figure 7 as an example, where Q_{OH} is modified). Another method is by varying the bond index. Recent DFT simulations have indicated that for certain classes of reactions good free-energy relations between the activation energy and heat of reaction exist.[30,31] Within the UBI−QEP framework, one can modify the arbitrary bond index of 0.5 to improve the accuracy of the predicted activation energies. We have actually explored this idea for the CO* + O* reaction on Pt,[19] motivated by DFT calculations and experiments. To alter the rate of the preferential CO + OH coupling reactions, here, the bond indices of R_{25} and R_{29} are modified to 0.8. The backward activation energy is calculated using the heat of reaction and the modified forward activation energy to maintain thermodynamic consistency. The activation energies of these reactions (both forward and backward) are increased by 3.6 and 3.2 kcal/mol, respectively, as a result of this change in bond indices. Note that such changes are well within the uncertainty of the UBI−QEP and DFT methods.

Microkinetic Modeling for CO Oxidation

J. Phys. Chem. B, Vol. 108, No. 39, 2004 **15255**

Figure 9b shows the predictions of the full mechanism (R_1–R_{46}) for the conditions of Figure 9a. The agreement of the predicted CO conversion and selectivity to CO oxidation with the corresponding experimental data is now better. A bond index of $\sim$0.6–0.65 is required when the modified pre-exponentials of R_9–R_{10}, R_{25}–R_{26}, and R_{29}–R_{30} are used. Results corresponding to Figure 8a (WGS) are also shown in Figure 8b with the modified bond indices. The mechanism captures the experimental data well with an A/V adjusted to 450 cm^{-1}. An A/V of $\sim$525 cm^{-1} is required when the modified pre-exponentials are used for R_9–R_{10}, R_{25}–R_{26}, and R_{29}–R_{30} and a bond index of $\sim$0.6–0.65 for R_{25} and R_{29}. From these results, it could be inferred that relatively subtle differences in the energetics of the microkinetic model can bring predictions into closer agreement with the experimental data, especially regarding the selectivity at very low CO conversion where small uncertainties result in large prediction errors.

Comparison of the UBI–QEP- and DFT-Based Energetics

In the development of the CO oxidation mechanism,[19] a bond index of 0.8 was used for the reaction step

$$CO_2^* + * \leftrightarrow CO^* + O^* \qquad (R_{23}–R_{24})$$

by comparing the energetics with experimental values and DFT calculations. A comparison of the activation energies in the H_2 oxidation chemistry with experimental values has previously been reported in ref 8 and is not repeated here. For the coupling reactions, here, we compare the energetics of the important steps, R_{29}–R_{32}, with the recent DFT calculations of Gong and Hu.[18] They estimated the energetics of these reactions within a H_2O^* + OH* mixed phase at $\theta_{CO} = 1/6$, $\theta_{OH} = 1/3$, and $\theta_{H_2O} = 1/3$. In their DFT calculations, CO* molecules were surrounded by hexagonal rings formed by H_2O^* and OH*. CO* reacts with one of the OH* to form COOH*. The decomposition pathways of COOH* were also studied in ref 18. Activation energies for R_{38} and R_{33} were studied in refs 32–33 using cluster calculations (low coverages). A comparison of the UBI–QEP-based activation energies at the DFT coverages and DFT values is shown in Table 1. The UBI–QEP-predicted energies are in fair agreement with the DFT calculations, given the uncertainty of both methods.

Additional DFT-based energetics or Bronsted–Evans–Polanyi (BEP)-type relationships for the coupling steps could be conducive for comparison or refinement of the semiempirical UBI–QEP-based activation energies. The roles of adsorbate–adsorbate interactions between CO- and H_2-related species could also be investigated using DFT calculations, especially for the effect of CO on the H_2O dissociation and disproportionation reactions. We leave these ideas for future work.

Conclusions

With an overall objective of developing a comprehensive surface reaction mechanism for WGS, PROX, and CH$_4$ POX and reforming of POX products on Pt, a thermodynamically consistent, optimized H_2 mechanism has been presented in the Appendix. The H_2/O_2 mechanism along with a CO oxidation mechanism on Pt was augmented with various coupling reaction pathways so that it can describe individual as well as simultaneous processes. Next, the reaction between CO and OH, whether through the direct or the indirect pathway, has been shown to be significant for predicting the promoting role of H_2O in the low-temperature CO oxidation, as well as the speed of the WGS and PROX data. Different scenarios (small changes in activation energies, pre-exponentials, heats of OH chemisorption, and bond indices) were explored to assess the role of uncertainties in the microkinetic model parameters on model predictions. It was found that, even with small uncertainties, the relative speeds of the direct and indirect (via carboxyl) pathways are close enough that one cannot definitively conclude which path is dominant under experimental conditions. With the parameters used here, it has been found that the direct oxidation path, CO* + OH* → CO$_2^*$ + H*, dominates over the indirect, carboxyl-based path, CO* + OH* → COOH* + $*$ → CO$_2^*$ + H*, in the water-promoted CO oxidation experiments. However, the indirect carboxyl paths, CO* + OH* → COOH* + $*$ and CO* + H_2O^* → COOH* + H*, play a vital role in the WGS and PROX simulations, with their relative roles varying with operating conditions. On the other hand, the formate path appears to be unimportant. Furthermore, the CO + OH reaction in conjunction with the promoting effect of hydrogen bonding on the H_2O disproportionation reaction, H_2O^* + O* → 2OH*, causes the low-temperature oxidation of CO in the presence of H_2O. Given the potential utilization of H_2O in reducing CO poisoning at low temperatures of PEM fuel cells, and the importance of WGS and PROX technologies in fuel processing and of POX for syngas production, the proposed microkinetic model could hopefully assist in the understanding and design of these processes.

Appendix: Development of a Surface Reaction Mechanism for H_2 Oxidation on Pt

In this appendix, we outline the development of a H_2/O_2 detailed, thermodynamically consistent reaction mechanism on Pt, along with its validation. The H_2/O_2 mechanism we will present, in conjunction with the CO/O$_2$ reaction mechanism of ref 19, forms the basis of the WGS and PROX reaction network discussed already.

Initial Pre-Exponentials and Heats of Chemisorption. Following refs 8 and 10, nine reversible reaction steps (R_1–R_{18}), treated as elementary, are proposed for H_2 oxidation on Pt. These steps are listed in Table 1. The multistep methodology for surface reaction mechanism development, introduced in refs 8 and 10, is adopted. In particular, order-of-magnitude estimates of the initial pre-exponentials are taken from the transition-state theory (TST) (10^{13} s^{-1} for desorption steps and 10^{11} s^{-1} for Langmuir–Hinshelwood reactions).[26] The pre-exponentials and sticking coefficients of the O$_2$ and O adsorption/desorption steps are those of the CO oxidation mechanism,[19] whereas the initial sticking coefficients for H_2, H, OH, and H_2O are the same as the initial ones reported in ref 10. The heats of chemisorption of all species and the adsorbate–adsorbate interactions, listed in Table 2, are those of refs 8 and 19, with the exception for the heat of H chemisorption that has been adjusted to 62 kcal/mol[8] to ensure enthalpic consistency.

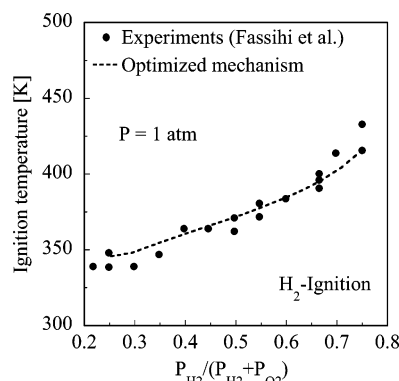**Coverage and Temperature Effects in Heats of Chemisorption and Activation Energies.** Interactions of 2.5 kcal/

Figure 10. Performance of the optimized H_2 mechanism against the H_2-ignition experiments of ref 40 performed at atmospheric pressure with ~94% N_2. The partial pressure of H_2 is varied while keeping the total pressure of H_2 and O_2 fixed at 45 Torr. Other parameters include a catalytic wire area of ~6.8×10^{-2} cm^2 and a reactor volume of ~62.4 cm^3. The residence time is adjusted to 3.2 s to approximate the transport limitations of the actual geometry with a simple CSTR model. The ignition temperature data is well captured by our optimized H_2 mechanism.

mol/ML between H_2O molecules are included to capture the coverage-dependent shift in the H_2O temperature-programmed desorption (TPD) spectra.[34] Michaelides and Hu performed periodic DFT calculations to study the autocatalytic effect of H_2O on H_2O formation.[35] They observed that the activation energy of R_9 ($H_2O^* + O^* \rightarrow 2OH^*$) decreases, and its reverse, R_{10}, increases in the presence of H_2O^*. Similarly, the activation energy of R_7 ($H_2O^* + * \rightarrow H^* + OH^*$) increases in the presence of OH^*. These changes in the activation energies of R_7-R_{10} in the presence of H_2O^* or OH^* may be attributed to attractive hydrogen-bonding interactions. We have found that an interaction of ~25 kcal/mol between H_2O^* and OH^* roughly captures the trends in DFT changes reported in ref 35, and we have used such an interaction in our mechanism (see Table 2). A similar magnitude of hydrogen-bonding interaction (~20 kcal/mol) between OH^* species was previously proposed in ref 36 to describe the increase in hydroxyl chemisorption energy at low coverages of oxygen. Cluster DFT and semiempirical UBI−QEP calculations show that the heat of OH chemisorption at low coverages is ~38−41 kcal/mol,[37] whereas periodic slab calculations and surface science experiments at high OH^* coverages show a typical value of ~59−61 kcal/mol,[38,39] where the increase is due to hydrogen bonding between OH moieties.

All activation energies are calculated using the UBI−QEP method.[23,24] The temperature dependence of the heats of chemisorption is estimated with statistical mechanics by accounting for the changes in translational, rotational, and vibrational DF upon adsorption (for details, refer to Table 2 and refs 11 and 19). The coverage- and temperature-dependent heats of chemisorption are summarized in Table 2. Such temperature dependence makes the activation energies also temperature dependent, an essential feature for ensuring enthalpic consistency as a function of temperature. The activation energies at 300 K are reported in Table 1. The mechanism with these parameters is hereafter denoted as the screening H_2 mechanism.

Experimental Data for Rate Parameter Optimization and Reactor Models. The pre-exponentials and sticking coefficients of the screening mechanism are unoptimized, and therefore, the mechanism predictions are semiquantitative or qualitative in nature. Their optimization against selected (targeted) experimental data is an important task to create quantitative reaction models. A variety of experimental data is available for H_2
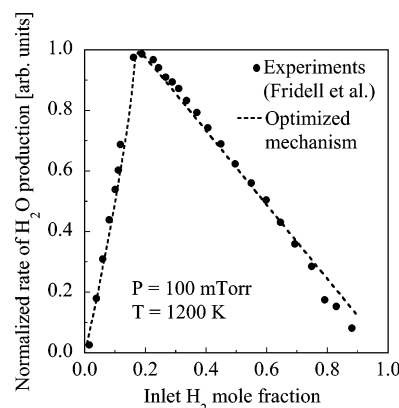

Figure 11. Performance of the optimized H_2 mechanism against the steady-state H_2O production experiments of refs 41 and 42 conducted at 100 mTorr and a temperature of 1200 K. Other parameters include a catalytic foil one-sided area of 0.66 cm^2 and a residence time of ~3.3 ms. Model predictions are normalized with the experimental peak rate (given in arbitrary units). The mechanism captures the experimental H_2O production rate well.
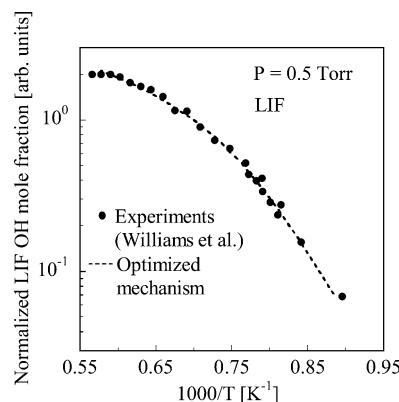

Figure 12. Performance of the optimized H_2 mechanism against the LIF OH-production experiments of ref 3 conducted at 0.5 Torr (0.2 Torr H_2O and 0.3 Torr O_2) over a temperature range ~1100−1800 K. Other parameters include a catalytic foil area of 0.51 cm^2 and a reactor volume of 0.4 L. Model predictions are normalized with the experimental data at the central temperature of 1430 K. The optimized H_2 mechanism captures the experimental OH mole fraction well.

oxidation on Pt. We have selected the atmospheric-pressure, low-temperature H_2 ignition experiments of ref 40; the low-pressure, high-temperature steady-state H_2O production experiments of refs 41−42; and the low-pressure, high-temperature laser-induced-fluorescence (LIF) OH production experiments of ref 3 as targeted experiments for optimizing the kinetic parameters of the screening H_2 mechanism. These experiments are chosen in order to cover different types of data over a wide range of operating conditions. These experiments were carried out on polycrystalline Pt (wires and foils). The experimental data are shown in Figures 10−12, and the operating conditions are summarized in the figure captions.

A continuously stirred tank reactor (CSTR) model is employed for these simulations. This is certainly a gross but common assumption.[3] The H_2 ignition experiments[40] are modeled using the robust two-parameter continuation algorithm of ref 43 to solve for the steady-state ignition temperature as a function of the inlet composition.

Optimization Strategy and Thermodynamic Consistency. The energetics in the screening H_2 mechanism are kept fixed, and only the pre-exponentials are optimized against the experimental data. The sticking coefficients of H_2, H, OH, and H_2O are allowed to vary between 5×10^{-3} and 1 (see refs 44−45

Microkinetic Modeling for CO Oxidation

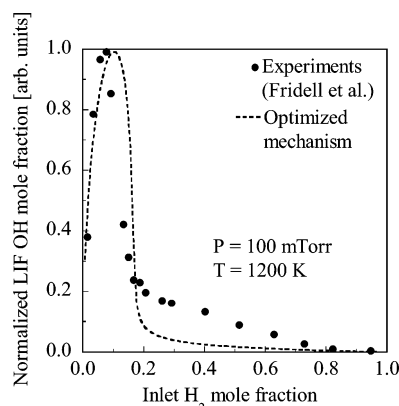*J. Phys. Chem. B, Vol. 108, No. 39, 2004* **15257**

Figure 13. Validation of the optimized H_2 mechanism against the LIF OH-production experiments of refs 41 and 42. The operating conditions are the same as in Figure 11. Model predictions are normalized with the experimental peak. The mechanism captures the experimental data fairly well.
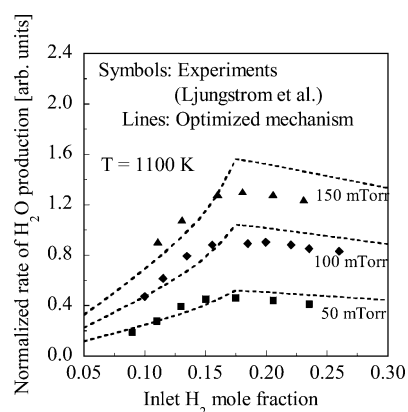

Figure 14. Validation of the optimized H_2 mechanism against the steady-state H_2O production experiments of ref 42 conducted at three different pressures of 50, 100, and 150 mTorr and a temperature of 1100 K. Other parameters include a Pt foil one-sided area of 0.75 cm^2 and a residence time of ~3.3 ms. Model predictions are normalized with the experimental rate (given in arbitrary units) at an inlet H_2 mole fraction of 0.16 and a pressure of 150 mTorr. The mechanism captures the experimental trends correctly.

for typical estimates), whereas the pre-exponentials are allowed to vary up to 2 orders of magnitude in each direction from their nominal TST value.

Even though enthalpic consistency is ensured using the UBI–QEP method and statistical mechanics, the screening H_2 mechanism is entropically inconsistent. This translates to differences between the equilibrium constants calculated using a gas-phase thermodynamic database (e.g., ref 46) and the rate parameters employed in the screening H_2 mechanism. As an example, an error up to a factor of ~165 over the temperature range 300–2000 K is observed. To ensure entropic consistency, the implicit thermodynamic constraints approach with a modified Arrhenius equation (denoted as case b in ref 11) is used in the optimization. The IMSL subroutine library[47] is employed for the optimization.

The optimized rate parameters of H_2 oxidation steps on Pt are shown in Table 1 (R_1–R_{18}), and this mechanism is hereafter denoted as the optimized H_2 mechanism on Pt.

Assessment of the Optimized H_2 Mechanism on Pt. Predictions using the optimized H_2 mechanism against the targeted experimental data are shown in Figures 10–12. The optimized H_2 mechanism captures the experimental data well. A thermodynamic consistency assessment of the optimized H_2 mechanism shows that the maximum deviation in the equilib-

rium constants over the temperature range 300–2000 K is ~44% with an average error of ~11%. Therefore, the optimized H_2 mechanism is reasonably thermodynamically consistent (lack of complete consistency results from the inadequacy of the modified Arrhenius expression to exactly capture the temperature effects over such a wide temperature range).

The mechanism is further validated against additional experimental data. Figure 13 shows the predictions using the optimized H_2 mechanism against the LIF OH production measurements of refs 41–42. Additional validation is carried out against the steady-state H_2O production experiments of ref 42 at three different pressures. The normalized predictions are shown in Figure 14. The optimized H_2 mechanism captures the correct trend in the H_2O production rate with changing pressure and is in reasonable agreement with the experimental data.

References and Notes

(1) Hickman, D. A.; Schmidt, L. D. *Science* **1993**, *259*, 343.
(2) Hickman, D. A.; Schmidt, L. D. *J. Catal.* **1992**, *138*, 267.
(3) Williams, W. R.; Marks, C. M.; Schmidt, L. D. *J. Phys. Chem.* **1992**, *96*, 5922.
(4) Hickman, D. A.; Schmidt, L. D. *AIChE J.* **1993**, *39*, 1164.
(5) Deutschmann, O.; Schmidt, R.; Behrendt, F.; Warnatz, J. *Twenty-Sixth Symposium (International) on Combustion*; The Combustion Institute: Pittsburgh, 1996; p 1747.
(6) Rinnemo, M.; Deutschmann, O.; Behrendt, F.; Kasemo, B. *Combust. Flame* **1997**, *111*, 312.
(7) Frauhammer, J.; Veser, G. *Chem.–Ing.–Tech.* **1998**, *70*, 1020.
(8) Park, Y. K.; Aghalayam, P.; Vlachos, D. G. *J. Phys. Chem. A* **1999**, *103*, 8101.
(9) Aghalayam, P.; Park, Y. K.; Vlachos, D. G. *Proc. Combust. Inst.* **2000**, *28*, 1331.
(10) Aghalayam, P.; Park, Y. K.; Vlachos, D. G. *AIChE J.* **2000**, *46*, 2017.
(11) Mhadeshwar, A. B.; Wang, H.; Vlachos, D. G. *J. Phys. Chem. B* **2003**, *107*, 12721.
(12) Kandoi, S.; Gokhale, A. A.; Grabow, L. C.; Dumesic, J. A.; Mavrikakis, M. *Catal. Lett.* **2004**, *93*, 93.
(13) Schubert, M. M.; Gasteiger, H. A.; Behm, R. J. *J. Catal.* **1997**, *172*, 256.
(14) Jacobs, G.; Williams, L.; Graham, U.; Thomas, G. A.; Sparks, D. E.; Davis, B. H. *Appl. Catal., A* **2003**, *252*, 107.
(15) Zhu, Y.; Uchida, H.; Watanabe, M. *Langmuir* **1999**, *15*, 8757.
(16) Robbins, J. L.; Marucchi-Soos, E. *J. Phys. Chem.* **1989**, *93*, 2885.
(17) Bergald, J.; Kasemo, B.; Chakarov, D. V. *Surf. Sci.* **2001**, *495*, L815.
(18) Gong, X.-Q.; Hu, P. *J. Chem. Phys.* **2003**, *119*, 6324.
(19) Mhadeshwar, A. B.; Vlachos, D. G. Submitted.
(20) Aghalayam, P.; Park, Y. K.; Fernandes, N. E.; Papavassiliou, V.; Mhadeshwar, A. B.; Vlachos, D. G. *J. Catal.* **2003**, *213*, 23.
(21) Petzold, L. R. *A description of DDASSL: a differential/algebraic system solver*; SAND82-8637; Sandia National Laboratories: Albequerque, NM, 1982.
(22) Mavrikakis, M. Personal communication, 2004.
(23) Shustorovich, E.; Sellers, H. *Surf. Sci. Rep.* **1998**, *31*, 1.
(24) Shustorovich, E. *Adv. Catal.* **1990**, *37*, 101.
(25) Deshmukh, S. R.; Mhadeshwar, A. B.; Vlachos, D. G. *Ind. Eng. Chem. Res.* **2004**, *43*, 2986.
(26) Dumesic, J. A.; Rudd, D. F.; Aparicio, L. M.; Rekoske, J. E.; Trevino, A. A. *The Microkinetics of Heterogeneous Catalysis*; American Chemical Society: Washington, DC, 1993.
(27) Xue, E.; Keeffe, M. O.; Ross, J. R. H. *Catal. Today* **1996**, *30*, 107.
(28) Morley, C. *GASEQ: Chemical equilibria in perfect gases*, version 0.75b; http://www.gaseq.co.uk.
(29) Kahlich, M. J.; Gasteiger, H. A.; Behm, R. J. *J. Catal.* **1997**, *171*, 93.
(30) Michaelides, A.; Liu, Z.-P.; Zhang, C. J.; Alavi, A.; King, D. A.; Hu, P. *J. Am. Chem. Soc.* **2003**, *125*, 3704.
(31) Norskov, J. K.; Bligaard, T.; Logadottir, A.; Bahn, S.; Hansen, E. W.; Bollinger, M.; Bengaard, H.; Hammer, B.; Sljivancanin, Z.; Mavrikakis, M.; Xu, Y.; Dahl, S.; Jacobsen, C. J. H. *J. Catal.* **2002**, *209*, 275.
(32) Anderson, A. B.; Neshev, N. M. *J. Electrochem. Soc.* **2002**, *149*, E383.
(33) Narayanasamy, J.; Anderson, A. B. *J. Electroanal. Chem.* **2003**, *554–555*, 35.
(34) Fisher, G. B.; Gland, J. L. *Surf. Sci.* **1980**, *94*, 446.
(35) Michaelides, A.; Hu, P. *J. Am. Chem. Soc.* **2001**, *123*, 4235.

(36) Patrito, E. M.; Olivera, P. P.; Sellers, H. *Surf. Sci.* **1994**, *306*, 447.

(37) Mhadeshwar, A. B.; Kragten, D. D.; Vlachos, D. G. *Proceedings of the Third Joint Meeting of the U.S. Sections of The Combustion Institute, Combustion Fundamentals and Application*; University of Illinois at Chicago: Chicago, March 16−19, 2003; www.cssci.org. Paper E02.

(38) Michaelides, A.; Hu, P. *J. Chem. Phys.* **2001**, *114*, 513.

(39) Anton, A. B.; Cadogan, D. C. *J. Vac. Sci. Technol.* **1991**, *9*, 1890.

(40) Fassihi, M.; Zhdanov, V. P.; Rinnemo, M.; Keck, K.-E.; Kasemo, B. *J. Catal.* **1993**, *141*, 438.

(41) Fridell, E.; Hellsing, B.; Kasemo, B.; Ljungstrom, S.; Rosen, A.; Wahnstrom, T. *J. Vac. Sci. Technol., A* **1991**, *9*, 2322.

(42) Ljungstrom, S.; Kasemo, B.; Rosen, A.; Wahnstrom, T.; Fridell, L. *Surf. Sci.* **1989**, *216*, 63.

(43) Kalamatianos, S.; Park, Y. K.; Vlachos, D. G. *Combust. Flame* **1998**, *112*, 45.

(44) van Santen, R. A.; Niemantsverdriet, J. W. *Chemical Kinetics and Catalysis*; Plenum Press: New York, 1995.

(45) Zhdanov, V. P. *Surf. Sci. Rep.* **1991**, *12*, 183.

(46) GRI Gas-Research-Institute mechanism for natural gas (3.0). http://www.me.berkeley.edu/gri_mech/ (accessed 1999).

(47) *IMSL FORTRAN subroutines for mathematical applications*; Visual-Numerics, Houston, TX, 1997.

(48) Burcat, A. Third Millennium Ideal Gas and Condensed Phase Thermochemical Database for Combustion, http://garfield.chem.elte.hu/Burcat/BURCAT.THR; Technion Aerospace Engineering (TAE) Report #867, January 2001.